THE JOURNAL OF PHYSICAL CHEMISTRY C
A JOURNAL OF THE AMERICAN CHEMICAL SOCIETY

pubs.acs.org/JPCC

Article

Pressure-Driven Symmetry-Preserving Phase Transitions in $Co(IO_3)_2$

A. Liang,* C. Popescu, F. J. Manjon, R. Turnbull, E. Bandiello, P. Rodriguez-Hernandez, A. Muñoz, I. Yousef, Z. Hebboul, and D. Errandonea

Cite This: J. Phys. Chem. C 2021, 125, 17448−17461

Read Online

ACCESS | Metrics & More | Article Recommendations | Supporting Information

ABSTRACT: High-pressure synchrotron X-ray diffraction studies of cobalt iodate, $Co(IO_3)_2$, reveal a counterintuitive pressure-induced expansion along certain crystallographic directions. High-pressure Raman and infrared spectroscopy, combined with density-functional theory calculations, reveal that with increasing pressure, it becomes energetically favorable for certain I−O bonds to increase in length over the full range of pressure studied up to 28 GPa. This phenomenon is driven by the high-pressure behavior of iodate ion lone electron pairs. Two pressure-induced isosymmetric monoclinic−monoclinic phase transitions are observed at around 3.0 and 9.0 GPa, which are characterized by increasing oxygen coordination of the iodine atoms and the probable formation of pressure-induced metavalent bonds. Pressure−volume equations of state are presented, as well as a detailed discussion of the pressure dependences of the observed Raman- and infrared-active modes, which clarifies previous inconsistencies in the literature.

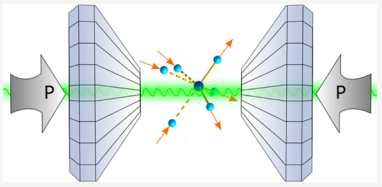

INTRODUCTION

Metal iodates, $M[IO_3]^-$, form a diverse range of non-centrosymmetric (NCS) materials, which exhibit useful and interesting properties such as non-linear optics;[1−3] visible to far-IR transparency (12.5 μm);[4,5] large second-harmonic generation coefficients;[5−8] a high optical damage threshold; and good thermal stability (up to 400 °C).[9,10] Consequently, the synthesis and behavior of metal iodates have been intensely studied under ambient conditions. In contrast, there remains a large deficit of studies of metal iodates under high-pressure (HP) conditions despite the clear possibility for new insights into pressure-induced effects,[11] in particular changes regarding the stereochemically active lone electron pair (LEP) of the iodate ion, $[IO_3]^-$.

Despite the scarcity of studies on iodates at HP in the literature, these have shown the potential for interesting physics of such compounds. For example, pressure-induced structural phase transitions have been observed in KIO_3 and $AgIO_3$,[12,13] and we recently reported HP studies on the structural and vibrational properties of transition-metal iodates $Fe(IO_3)_3$ and $Zn(IO_3)_2$,[14−16] in which we observed both first- and second-order phase transitions driven by increasing atomic coordination of the iodine atoms. Even though $Fe(IO_3)_3$ and $Zn(IO_3)_2$ are not isostructural, they exhibit similar HP phenomena, thus providing motivation to explore the HP behavior of other metal iodates. Cobalt iodate, $Co(IO_3)_2$, is a noteworthy candidate because cobalt is the next element in the periodic table after iron, and, until the present study, no HP data on the structural or vibrational properties of $Co(IO_3)_2$ were available.

The LEP of the iodate ion plays an important role in the HP phenomena reported herein. In the $[IO_3]^-$ ion, the iodine atom (electronic configuration $5s^25p^5$) shares its p-electrons with the oxygen atoms, thus leaving the pair of 5s electrons stereochemically active. In particular, they are oriented along the *b*-axis in the $Co(IO_3)_2$ crystal structure.[17] The $Co(IO_3)_2$ crystal structure is shown in Figure 1. Under ambient conditions, $Co(IO_3)_2$ crystallizes in the monoclinic space group $P2_1$ (S.G. no. 4) with the following unit-cell parameters: a = 10.939(1) Å, b = 5.071(1) Å, c = 10.936(1) Å, and β = 119.95(1)°.[17] The $[Co]^{2+}$ cations are coordinated to six O atoms and form slightly distorted octahedral CoO_6 units, which are connected by IO_3 triangular pyramids. Each CoO_6 unit is surrounded by six IO_3 groups. When viewed perpendicular to the *b*-axis, the crystal structure of $Co(IO_3)_2$ is constituted by layers of IO_3 units parallel to the *ac*-plane (Figure 1b). The crystal structure of $Co(IO_3)_2$ is similar to that of $Zn(IO_3)_2$; however, its unit-cell is doubled. Consequently, the vibrational spectrum of $Co(IO_3)_2$ is more complex than that of $Zn(IO_3)_2$. Raman and infrared (IR) spectra of $Co(IO_3)_2$ under ambient conditions were reported by Pracht and Lutz[18] and Kochuthresia et al.[19]

Using X-ray diffraction (XRD) and vibrational spectroscopy experiments combined with density functional theory (DFT) calculations, we report here two subtle pressure-induced phase transitions in $Co(IO_3)_2$ at 3 GPa and in the range 9.0−11.0 GPa, respectively. The evolution of the unit-cell parameters under pressure up to 27 GPa reveals a counterintuitive expansion along the *a* and *c* axes in both the lower pressure

Received: May 27, 2021
Revised: July 2, 2021
Published: July 29, 2021

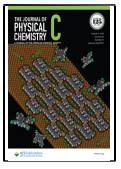

https://doi.org/10.1021/acs.jpcc.1c04659
J. Phys. Chem. C 2021, 125, 17448−17461

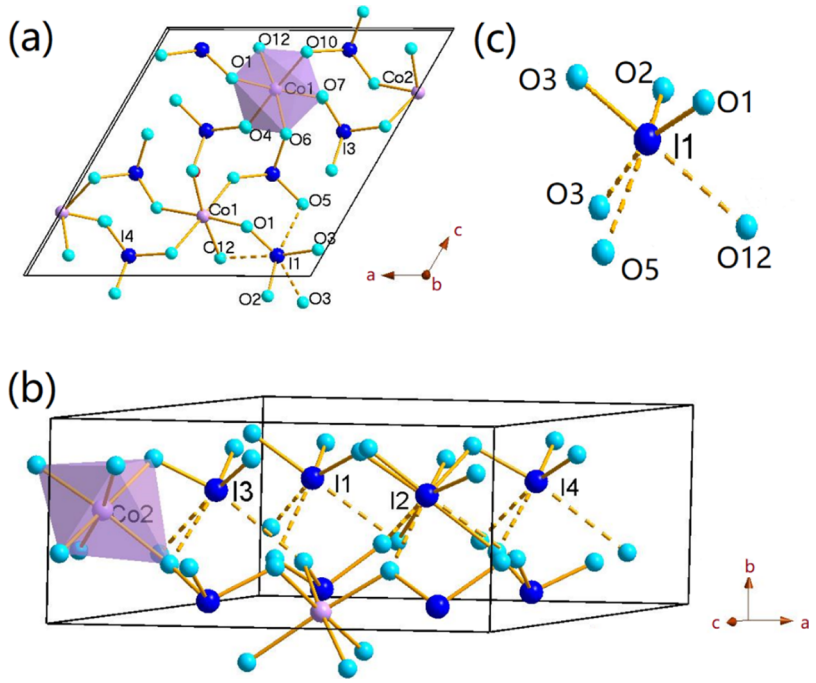

Figure 1. Crystal structure of $Co(IO_3)_2$ (a) along the *b*-axis and (b) perpendicular to the *b*-axis at ambient pressure. (c) Detail of the $I1O_6$ unit in (b). In the structure, the atoms are labeled. Solid yellow lines represent the bonds at ambient pressure. Dashed yellow lines, between iodine and the oxygen in the neighbor IO_3 units, represent the bonds that gradually form at high pressure. The detail of the iodine coordination change can be found in the article.

Table 1. $Co(IO_3)_2$ Lattice Parameters as Refined from Experimental Data and as Calculated by DFT

	a (Å)	b (Å)	c (Å)	β (deg)	V_0 (Å^3)
experiment	10.943(6)	5.078(1)	10.925(4)	119.814(3)	526.68(4)
calculation (PBEsol)	10.827	4.962	10.794	119.443	505.00
calculation (AM05)	10.761	5.171	10.796	119.095	525.00

phases (ambient-pressure and I1 phase) below 9−11 GPa, and the change found both in *a* and *c* axes were underpinned by the HP behavior of the LEP of the iodate ion. We show that increasing the I−O bond lengths in certain crystallographic directions becomes energetically favorable at HP in order to accommodate the formation of additional I−O bonds. The bond lengthening is confirmed by the Raman and IR spectroscopies as well as the DFT calculations. Birch−Murnaghan pressure−volume equations of state are presented along with the pressure dependence of the Raman- and infrared-active modes, their pressure coefficients, and the Grüneisen parameters at zero pressure. Also, symmetries are assigned to the optical modes. A critical comparison is made with other iodates.

METHODS

Sample Synthesis. Micron-sized needle-like crystals of $Co(IO_3)_2$ were synthesized from an aqueous solution of sodium iodate $NaIO_3$ (2 mmol, 98% purity, Fluka) and cobalt chloride $CoCl_2$ (1 mmol, 97% purity, Sigma-Aldrich) in de-ionized water, in which the following reaction took place: $2NaIO_3 + CoCl_2 \rightarrow Co(IO_3)_2 + 2NaCl$. The reaction mixtures were slowly evaporated at 60 °C for 4 days, leading to the precipitation of purple needle-like crystals, which were filtrated and washed with de-ionized water.

The particle size, morphology, and chemical composition of the samples were assessed using a scanning electron microscope with a Peltier cooled XFlashTM silicon drift detector (model 410 M) for energy-dispersive X-ray (EDX) analysis. The analysis was performed using 20 keV primary electrons. SEM images of the $Co(IO_3)_2$ crystal morphology are shown in Figure S1 in the Supporting Information. The results from the EDX analysis are also shown in Figure S2 in the Supporting Information. Within the limits of experimental errors, only Co and I were detected. The weight percent and atomic percent of Co and I agree with the expected molar ratio of 1:2.

XRD at Ambient Pressure. Ambient-pressure powder XRD measurements were performed to identify the purity and the crystal structure of $Co(IO_3)_2$ using an X'Pert Pro diffractometer from Panalytical (Cu K_α radiation). The corresponding XRD data are shown in Figure S3 in the Supporting Information. The data were refined by the Rietveld method.[20] The structure information of $Co(IO_3)_2$ reported by Phanon et al.[17] was used as a model for the refinement. The unit-cell parameters and volume obtained from our refinement are shown in Table 1 and are in good agreement with the values reported by Phanon et al.[17] Moreover, the values reported here are close to the unit-cell parameters and volume obtained from our DFT calculations at 0 GPa (see Table 1). We refer the reader to the calculation details section to know more about the PBEsol and AM05 functionals. In the refinement, shown in Figure S3 in the Supporting Information, the positions of the observed and calculated reflections are well matched. The difference in observed and calculated intensities between 35° and 70° is caused by the partially preferred

https://doi.org/10.1021/acs.jpcc.1c04659
J. Phys. Chem. C 2021, 125, 17448−17461

direction of the needle-like crystals. The same issue has been previously detected for $Zn(IO_3)_2$ crystals synthesized by a similar chemistry method.[16] No impurity or other phases were detected by XRD.

***In Situ* XRD at High Pressure.** Angle-dispersive powder HP-XRD was performed at the BL04-MSPD beamline of ALBA synchrotron.[21] An incident monochromatic X-ray beam with a wavelength of 0.4246 Å was focused down to a spot size of 20 μm × 20 μm. Diffraction data were recorded using a Rayonix SX165 CCD detector. The two-dimensional diffraction images were integrated into one-dimensional intensity versus 2θ patterns using Dioptas.[22] The sample-to-detector distance along with detector orientation parameter were refined using diffraction data from a LaB_6 calibrant. The $Co(IO_3)_2$ sample was loaded into a membrane-driven diamond-anvil cell (DAC) with diamond culets of 400 μm using a T301 stainless-steel gasket, pre-indented to a thickness of 40 μm and with a sample chamber of 180 μm diameter in the center, drilled via spark erosion. A 16:3:1 methanol/ethanol/water mixture was used as the pressure-transmitting medium (PTM) and pressure was determined using the equation of state of gold.[23]

High-Pressure Fourier Transform Infrared. FTIR measurements were conducted at ALBA synchrotron at the BL01-MIRAS beamline. $Co(IO_3)_2$ was loaded in a DAC designed for IR microspectroscopy equipped with IIAC-diamonds (300 μm culet size). A stainless-steel gasket pre-indented to a thickness of 40 μm and with a 150 μm diameter hole in the center was used as a pressure chamber. Cesium iodide (CsI) was used as the PTM because it provides the widest IR transmission window amongst the possible PTMs.[24] The sample pressure was determined using the ruby scale.[25] The FTIR−microspectroscopy experiments were performed in transmission mode using a masking aperture size of 45 × 45 μm^2 and a beam current inside the synchrotron ring of 250 mA. More details on the experimental set-up of the MIRAS beamline can be found elsewhere.[26]

Raman Spectroscopy. High-pressure Raman spectroscopy (HP-RS) measurements were carried out with a Horiba Jobin Yvon LabRAM HR UV microspectrometer using a 632.8 nm He/Ne laser light source. A thermoelectrically cooled multichannel CCD detector was used to collect the signal and the spectral resolution was better than 2 cm^{-1}. The set-up was calibrated using He plasma lines before the HP-RS experiment. $Co(IO_3)_2$ crystals and ruby chips were loaded in a 250-μm hole of a pre-indented steel gasket (thickness of 45 μm) inside a membrane-driven DAC. The PTM used in HP-RS experiments was a 4:1 methanol/ethanol mixture, and the ruby fluorescence method was used for pressure calibration.[25]

First-Principles Calculations. *Ab initio* calculations of the structural, electronic, dynamical, and elastic properties were performed in the framework of DFT.[27] We used the Vienna ab initio simulation package.[28,29] The projector-augmented wave[30] pseudo-potentials method was used, with a 540 eV plane-wave cutoff to ensure high accurate convergence. The Brillouin zone k-point integration was carried out using a significant sampling of a 4 × 6 × 4 grid for the primitive unit cell. We employed the generalized-gradient approximation with both the Perdew, Burke, and Ernzerhof for solids (PBEsol)[31] and the Armiento and Mattsson (AM05)[32] prescription for the exchange−correlation energy. Additionally, we performed our simulations with the DFT + U scheme of Duradev et al.[33] to treat the strongly correlated states of the Co atom through a single effective parameter, $U_{eff} = U - J$, where U and J are the screened Coulomb and exchange parameters, respectively. The selected value of U_{eff} was 3.32 eV for the Co atoms.[34] The antiferromagnetic configuration was found to be lowest in energy. The cell parameters and the atomic positions were relaxed to obtain the optimized configurations for a given volume, where the atomic forces were less than 0.004 eV/Å, and the stress tensor was diagonal to within an accuracy of more than 0.1 GPa. This procedure allowed us to obtain a set of volumes, energy, and pressure from our simulations, which were fitted with an equation of state to obtain the equilibrium volume, bulk modulus, and pressure derivative. To perform the lattice-dynamics calculations, we used the Phonopy package[35] to obtain the wavenumbers and the eigenvectors of the normal vibrational modes at the Γ point and its irreducible representations.

RESULTS AND DISCUSSION

HP-XRD Measurements. Selected HP-XRD patterns are presented in Figure 2. The Miller indices of the corresponding

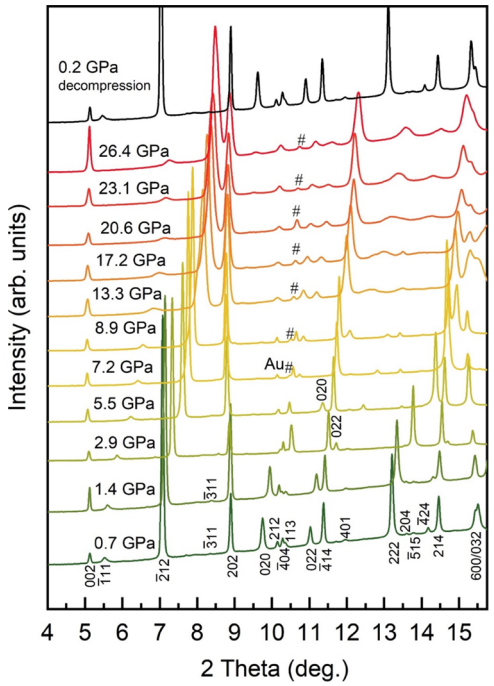

Figure 2. HP-XRD spectra of $Co(IO_3)_2$ at selected pressures. The top pattern was collected during the decompression process.

reflections are indicated. Under compression, most of the observed Bragg reflections shift to higher angles, indicating a pressure-induced decrease of the interplanar spacings. Some of the observed $Co(IO_3)_2$ reflections are more sensitive to pressure than others and therefore shift at different rates. For example, (020) is more sensitive to pressure than $(\bar{4}14)$, resulting in a pressure-induced crossing of the reflections (Supporting Information, Figure S4a). Interestingly, some of the reflections shift to lower Bragg angles with increasing pressure, for example (202), thereby indicating a pressure-induced increase in the corresponding interplanar spacing. This strongly non-isotropic behavior results in the merging of some of the observed reflections at HP, most notably those above 14°. Pressure-induced reflection broadening occurs above 10 GPa, that is, beyond the hydrostatic limit of the

https://doi.org/10.1021/acs.jpcc.1c04659
J. Phys. Chem. C 2021, 125, 17448−17461

PTM.[36,37] All these changes are reversible, as demonstrated by comparison of the top XRD pattern (acquired after sample decompression to 0.2 GPa) and the bottom XRD pattern (acquired upon commencing sample compression to 0.7 GPa). Over the entire pressure range of the experiments, no new reflections are observed, nor do any of them disappear. Therefore, all acquired XRD patterns can be indexed using the monoclinic $P2_1$ (SG no. 4) ambient-pressure structure and the Rietveld refinement of the XRD data at selected pressure can be found in the Supporting Information (Figure S5).

The pressure evolution of the unit-cell parameters (a, b, c, and β) was determined via the Le Bail method[38] and it is shown in Figure 3. The top panel of Figure 3 shows the

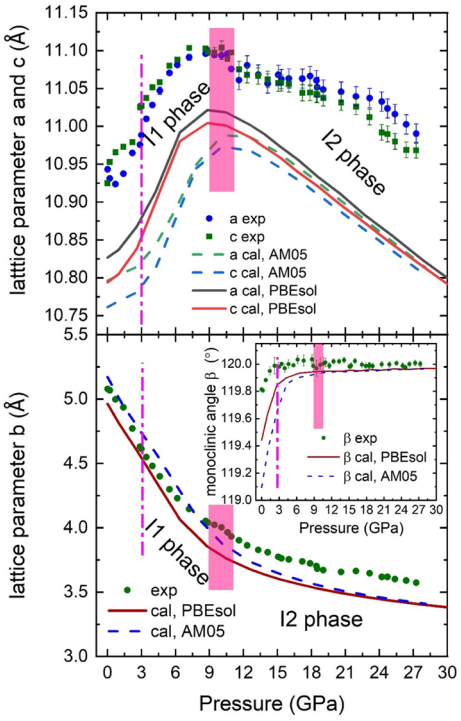

Figure 3. Pressure dependence of the unit-cell parameters. The inset is the pressure dependence of the monoclinic angle, β. The error of lattice parameter b is smaller than the symbol. Squares and circles correspond to experimental (exp) data while lines correspond to the calculated (cal) data (PBEsol-solid lines and AM05-dashed lines). The vertical pink dashed line and pink rectangle indicate the phase transition pressure or transition pressure region in the experiment and DFT calculation, respectively.

pressure dependence of the a- and c-axes. The values extracted from the experimental data are compared with those of DFT calculations performed using different exchange−correlation functionals: PBEsol and AM05. The experiments and calculations give similar results, whereby both a and c initially exhibit a slight increase upon compression from ambient pressure to 3.0 GPa, followed by a more abrupt increase in the pressure range of 3.0−9.0 GPa, and by a general decrease from 11.0 GPa to the highest pressure reached (27.0 GPa). This non-linear behavior of the unit-cell parameters is magnified in Figure S4b in the Supporting Information, where we report the pressure dependence of the d-spacing corresponding to peak (202). The non-linear behavior of the lattice parameters a and c is qualitatively similar to that observed in $Zn(IO_3)_2$.[16] Notice that a different setting (unique axis) was used to describe $Zn(IO_3)_2$ and $Co(IO_3)_2$ in the literature.[16,17] For the sake of simplicity, we will here describe both structures with the same setting using the b-axis as the unique axis, as recommended by the International Union of Crystallography. The non-linear behavior of unit-cell parameters in $Zn(IO_3)_2$[16] was identified as an evidence of the presence of symmetry-preserving phase transitions. For the sake of comparison, we have included in Figures S6−S10 in the Supporting Information the pressure evolution of the normalized lattice parameters and unit-cell volumes of $Co(IO_3)_2$ of this work and of $Zn(IO_3)_2$.[16]

Compressibility. In $Co(IO_3)_2$, a discontinuity in the compressibility of a and c lattice parameters and that of the b lattice parameter and unit-cell volume, as discussed later in the article, have been identified at 3.0 and in the 9.0−11.0 GPa range. The discontinuities are denoted by vertical dashed lines and the rectangles are shown in pink in Figure 3. The two HP phases are herein referred to as I1 and I2 (where "I" signifies that the phases are "isosymmetric"). The onset pressures of the two phase transitions in $Co(IO_3)_2$ are slightly higher than those observed in $Fe(IO_3)_3$ (in which similar transitions happen at 1.5−2.0 and 5.7−6.0 GPa)[14] and they are similar to those observed in $Zn(IO_3)_2$ (in which they occur at 2.5−3.4 and 8.9 GPa).[16] Qualitatively similar transitions have also been found in the iodate $Na_3Bi(IO_3)_6$.[39] Therefore, we suggest that symmetry-preserving transitions are a typical feature of metal iodates under compression.

Regarding the b lattice parameter, we found that its evolution under pressure is different from that of the a and c lattice parameters (see Figure 3). The b lattice parameter exhibits a conventional behavior in that it decreases under compression. Nonetheless, it is found to be very sensitive to pressure. The lattice parameter b shrinks drastically from 5.08 Å at ambient pressure to 3.57 Å at 27.2 GPa, thereby exhibiting a reduction of 29.7% in experiments (32.0% reduction in calculation using PBEsol and 34.1% reduction in calculation using AM05). Two discontinuities can be observed in the data, as shown in Figure 3, which correspond to the transition pressures discussed before in the context of the a and c lattice parameters. The relative change with pressure of the b-axis is dramatic compared with those of the a- and the c-axes, with both shrinking less than 2% in the same pressure range. Consequently, $Co(IO_3)_2$ exhibits significant anisotropic compressibility under pressure, with the b-axis exhibiting by far the largest zero-pressure compressibility of the three axes.

In order to explain the highly anisotropic compressibility of $Co(IO_3)_2$, it is necessary to recall that the LEPs of the $[IO_3]^-$ tetrahedra point along the b-axis direction (Figure 1b). At low pressures, the iodine atom only bonds with the three oxygen atoms on the top, leaving a layer of LEPs in the a−c plane. This "soft" layer of LEPs between the layers of $[IO_3]^-$ units is very sensitive to pressure, resulting in the higher compressibility of the b lattice parameter at low pressures. In contrast, the a and c axes consist of chains of CoO_6 octahedra and IO_3 polyhedra, which clearly leads to a lower compressibility along those directions. Notably, lattice parameters calculated using the PBEsol functional to describe the exchange−correlation energy show a better agreement with experimental data than those obtained using the AM05 functional.

For the monoclinic angle, β, we found that it increases from 119.82° at ambient pressure to around 120° at 3 GPa, when it becomes roughly constant within experimental accuracy above this pressure (see the inset in Figure 3). A similar behavior has also been found in the pressure dependence of the monoclinic

https://doi.org/10.1021/acs.jpcc.1c04659
J. Phys. Chem. C 2021, 125, 17448−17461

angle of $Zn(IO_3)_2$[16] (see Supporting Information, Figure S9). Based on the negligible difference between *a* and *c* lattice parameters for $Co(IO_3)_2$ in the I2 phase (for instance, only 0.02 Å at the highest pressure) and on the 120° value of the β angle, we hypothesize that the symmetry of the I2 phase would follow a martensitic transformation from monoclinic to hexagonal under compression.

Coordination Change. In order to better understand the nature of the two observed phase transitions and the compressional anisotropy observed in the lattice parameters of $Co(IO_3)_2$, we now focus on the Co−O and I−O bond distances which underpin those observations. For that purpose, we have plotted in Figures 4 and 5 the theoretical pressure

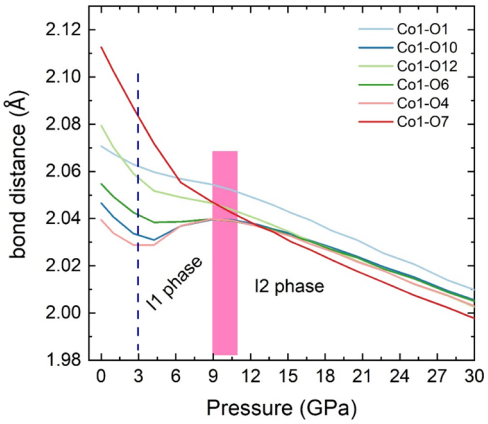

Figure 4. Theoretical (PBEsol) pressure dependence of the different Co1−O bond distances. The position of the atoms in this figure are shown in Figure 1. The vertical dashed line and rectangles indicate the isosymmetric phase transitions.

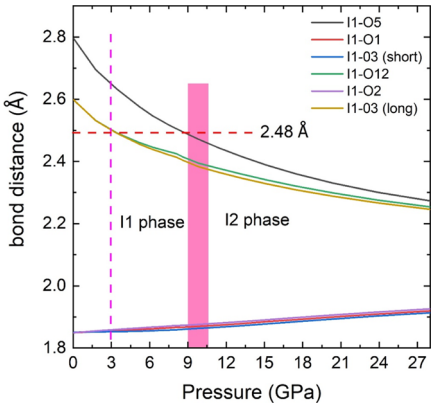

Figure 5. Theoretical (PBEsol) pressure dependence of the different I1−O bond distances. The atomic position atoms in this figure correspond to atoms labeled in Figure 1. The vertical dashed line and rectangles indicate the isosymmetric phase transitions.

dependence of Co1−O and I1−O bond distances as representative examples of the bond distances in all Co- and I-centered polyhedrals since the different Co coordination polyhedra within the $Co(IO_3)_2$ structure exhibit a very similar behavior (the same can be stated for the different I coordination polyhedra). Note that bond distances have been named using the nomenclature of Phanon et al.[17]

In Figure 4, all Co−O bond distances exhibit a similar pressure-induced behavior in that they all shorten under compression in both the ambient-pressure phase and in the I2 phase. Unusually, some of the bond distances increase with pressure in the I1 phase. Consequently, over the pressure range studied (0−28 GPa), some of the Co1−O bond distances show an s-like, non-linear behavior which supports the phase transitions observed in the lattice parameter evolution. The non-linear behavior also can be found in the distortion index change of $Co1O_6$ polyhedra (Supporting Information, Figure S11) calculated by VESTA.[40] The function used to calculate the distortion index can be found elsewhere.[16] Under compression, the CoO_6 polyhedra gradually become more symmetric. The distortion index of CoO_6 decreases from 0.01 at 0 GPa to 0.003 at around 10 GPa and then further to 0.0009 at 29 GPa, thus becoming essentially a regular octahedron.

In order to study I-centered polyhedra, we have taken IO_6 units. We consider a 3 + 3 coordination of iodine because the original IO_3 polyhedron at ambient pressure (I atoms link to only three O atoms) changes at high pressure to link three additional O atoms from neighboring IO_3 units, thus forming two types of bonds (see Figure 5): the original shorter strong bonds and longer weak I−O bonds. These two types of bonds have lengths of around 1.8−1.9 and 2.6−3.0 Å, respectively (see Figure 1). In Figure 5, we show the pressure dependence of the I1−O bond distances inside the IO_6 polyhedron. The three first-neighboring oxygen atoms [I1−O2, I1−O3(short), and I1−O1] behave very differently from the three second-neighboring oxygen atoms [I1−O5, I1−O12, and I1−O3-(long)]. The first-neighbor distances increase under compression, while the second neighbor distances rapidly decrease. If we consider 2.48 Å (a value 25% larger than the shortest I−O distance[16,41]) as the maximum bonding distance or coordination distance, indicated by a horizontal pink dashed line in Figure 5, then there is a gradual increase in iodine coordination under compression. It can be observed that, as the IO_3 LEPs are pushed closer to the oxygen atoms in the next layer of IO_3 units at HP, they form new I−O bonds and the *b*-axis becomes shorter, thus decreasing the length of the new I−O bonds. In contrast, the bond distance between iodine and the original three first-neighbor oxygen atoms increases under compression to accommodate the additional oxygen atoms. It has been observed that the enlargement of the short I−O bonds induces the softening of high-wavenumber vibrational modes in $Zn(IO_3)_2$ and $Fe(IO_3)_3$ at HP.[14,16] We will show in the next sections that the same phenomenon is observed in HP-RS experiments of $Co(IO_3)_2$. The subtle dynamic instability of the crystal lattice observed for $Fe(IO_3)_3$, indicated by the small negative frequency near the Γ-point in the theoretical calculated phonon dispersion curves, caused by the gradual increase of iodine coordination and the enlargement of the short I−O bonds, is likely also the reason triggering the two isostructural phase transitions in $Co(IO_3)_2$. The gradual increase of iodine coordination is related to the decrease of the stereoactivity of the LEP at HP as found in many compounds with strong LEP stereoactivity.[11,39] This conclusion is based on the fact that we detect the two phase-transitions according to the behavior of the lattice parameters simultaneously with the increase of the coordination of iodine. Unlike the non-linear distortion index curve of the CoO_6 units under pressure (Supporting Information, Figure S11), the distortion index of IO_6 units decreases continuously from 0.18 at 0 GPa to 0.08 at 29 GPa, whereby the IO_6 polyhedron becomes more symmetrical with pressure.

Equation of State. The unit-cell volume of $Co(IO_3)_2$ is shown as a function of pressure in Figure 6. Third-order

https://doi.org/10.1021/acs.jpcc.1c04659
J. Phys. Chem. C 2021, 125, 17448−17461

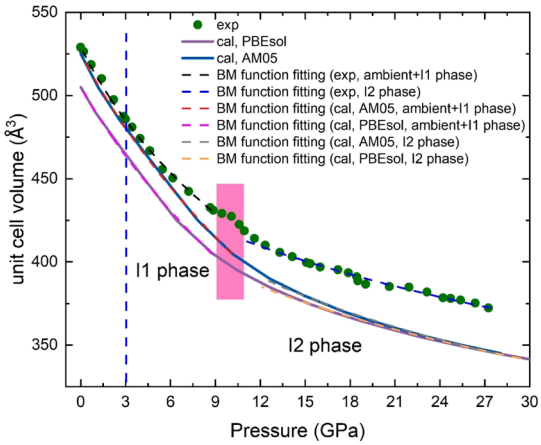

Figure 6. Isothermal equation of state of $Co(IO_3)_2$ at room temperature. The solid green circle and the solid line are the experimental and calculated volumes, respectively. The error of unit-cell volume is smaller than the symbol. Dashed color lines were used for the Birch–Murnaghan[42,43] function fitting on the experimental data and calculated data, respectively. The vertical dashed line and rectangle are the indication of the phase transition.

Birch–Murnaghan (BM) equations of state[42,43] were used to fit the volume of different phases separately using EoSFit7c.[44] Notice that it is impossible to fit the data over the whole pressure range with only one equation of state, which also supports the existence of isostructural phase transitions. Considering that no noticeable discontinuity is observed between the ambient-pressure and I1 phases and that there are no sufficient data for the ambient-pressure phase to fit the BM equation, we fit those two phases together with only one equation of state, where the zero-pressure volume was fixed. On the other hand, the zero-pressure volume was left as a free parameter during the fitting procedure for the I2 phase. The obtained zero-pressure volume (V_0), bulk modulus (B_0), and its pressure derivative (B_0') of those two regions (experiment and calculations) are summarized in Table 2. The close agreement between the experimental and calculated bulk modulus with the PBEsol functional for the different phases reflects the reasonable description of the equation of state by *ab initio* calculations. In contrast, with the previously reported metal iodates, the experimental bulk modulus of the ambient-pressure + I1 phase (29.8 GPa) is a little higher than that of the ambient-pressure phase of KIO_3 (24.3 GPa)[12] and $Zn(IO_3)_2$ (21.6 GPa).[16] On the contrary, the I2 phase of $Co(IO_3)_2$ is one of the least compressible metal iodates observed to date according to the values in the literature (70.8(3.6) GPa).

Interestingly, the experimental bulk modulus of the low pressure phase of $Co(IO_3)_2$ is lower than that of $Fe(IO_3)_3$ (55 GPa),[15] $LiIO_3$ (34 GPa),[45] and $LiZn(IO_3)_3$ (55 GPa).[46] Additionally, fitting a third-order BM equation of state to the calculated $Co1O_6$ and $I1O_6$ polyhedra in the ambient and I1 phases gives us polyhedral bulk moduli of B_0 = 102(14) GPa and 22(1) GPa, respectively. Thus, it is clear that the bulk modulus of $Co(IO_3)_2$ is dominated by the higher compressibility of IO_6 polyhedra rather than by the harder CoO_6 octahedra. The same behavior has also been observed in the theoretical data of iron and zinc iodates under pressure,[15,16] whose bulk moduli have also been shown to be dominated by the compressibility of the IO_6 polyhedra (where we assume a similar 3 + 3 coordination of iodine) rather than that of the AO_6 polyhedra where A represents a metal atom. The drastic increase of the bulk modulus after the transition to the HP I2 phase observed in this work on $Co(IO_3)_2$ is a consequence of the decrease of the compressibility of the coordination polyhedron of iodine.

Raman Study. In Figure 7, we present the Raman spectrum of $Co(IO_3)_2$ measured under ambient conditions.

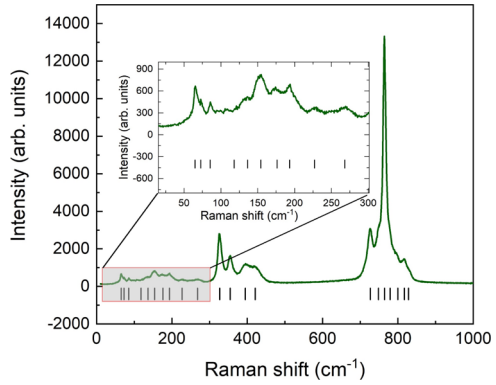

Figure 7. Raman spectrum of $Co(IO_3)_2$ at ambient pressure. Short vertical bars at the bottom of the spectra are an indication of the determined peak position. The insert spectrum is a zoom of the wavenumber range 0–300 cm^{-1}.

The determined Raman peaks are indicated with vertical bars, and the zero-pressure wavenumbers are listed in Table 3 along with their pressure coefficients and Grüneisen parameters. The zero-pressure wavenumbers are also compared with the data reported in the literature.[18,19] A tentative assignment of the symmetries of the modes' symmetries is provided in Table 3 based on a comparison of the calculated and experimental ambient pressure wavenumbers (ω_0) and pressure coefficients ($d\omega_0/dP$), which were determined via linear fit to the data for pressures smaller than 3 GPa.

Here, we only focus on the calculations performed with the PBEsol functional because of the better agreement with experimental data in the structural part of the work. The agreement between calculations and experiments is similar to that found in $Fe(IO_3)_3$ and $Zn(IO_3)_2$.[14,16] As in previous metal iodates calculations, our simulations underestimate the measured wavenumbers, especially of the high-wavenumber modes (wavenumber offset is around 70 cm^{-1} in the high-wavenumber range), thus underestimating the phonon gap

Table 2. Equation of State of $Co(IO_3)_2$ as Determined by Experiments and by Theoretical Calculations

	ambient + I1 phase			I2 phase		
data source	V_0 (Å3)	B_0 (GPa)	$B0'$	V_0 (Å^3)	B_0 (GPa)	$B0'$
experiment	529	29.8(1)	3.5(0.3)	462.9(5.6)	70.8(3.6)	5.2(0.6)
calculation (PBEsol)	505	32.1(1.1)	2.3(0.3)	451.1(2.6)	50.7(1.6)	5.5(0.3)
calculation (AM05)	525	30.7(0.6)	2.2(0.1)	473.7(4.9)	38.3(1.9)	5.4(0.4)

https://doi.org/10.1021/acs.jpcc.1c04659
J. Phys. Chem. C 2021, 125, 17448–17461

Table 3. Theoretical and Experimental Raman- and IR-Active Zero-Pressure Wavenumbers (ω) for $Co(IO_3)_2$ (the Lowest Pressure in the Infrared Spectroscopy Experiment Is 0.2 GPa) and Pressure Coefficients ($d\omega/dP$)[a]

	theory (B_0 = 32.1 GPa)			experiment, Raman (B_0 = 29.8 GPa)					experiment, IR (B_0 = 29.8 GPa)			
modes	ω (cm^{-1})	$d\omega/dP$ (cm^{-1}/GPa)	γ	ω (cm^{-1}), this work	$d\omega/dP$ (cm^{-1}/GPa)	γ	ω (cm^{-1})[18]	ω (cm^{-1})[19]	ω (cm^{-1}), This work	$d\omega/dP$ (cm^{-1}/GPa)	γ	ω (cm^{-1})[19]
B	62.3	0.3	0.16	65								
A	71.9	4.3	1.91	73	5.4	2.21						
A	91.70	4.0	1.39	85	6.8	2.39	84	85				
A	117.9	2.5	0.68	118	11.0	2.79		115				
B	136.3	4.5	1.05	136	9.7	2.13	135	135				
A	161.38	3.9	0.78	154	11.1	2.15	153	154				
A	155.5	5.0	1.03						162	9.8	1.80	161
B	173.7	6.9	1.27	176	8.1	1.37	172	167	172	9.6	1.66	171
B	184.4	6.2	1.07						186	12.3	1.97	
A	196.8	5.6	0.91	193	6.2	0.96	191	192				
A	221.2	5.6	0.81	227	9.9	1.29	224	231	231	6.7	0.86	227
A	246.5	6.6	0.86						268	4.2	0.47	267
A	251.0	8.5	1.09	268	7.8	0.87	265	266				
B	311.2	4.8	0.49	327	6.5	0.59	327	327				
B	333.6	2.4	0.23						331	1.4	0.13	327
A	344.5	6.6	0.62	354	7.4	0.62	353	353				
B	358.5	6.0	0.53						357	1.8	0.15	355
B	385.2	3.7	0.31						397	4.1	0.31	399
A	387.8	5.3	0.44	395	5.0	0.37	394	392				
A	412.6	7.3	0.57	421	4.8	0.34	409	429				
B	429.8	4.9	0.36						427	5.7	0.40	421
A	670.2	−3.8	−0.18	727	−4.0	−0.16	727	727				
B	677.1	−3.4	−0.16	748	−3.8	−0.15	750					
A	720.1	−1.7	−0.08	765	−1.2	−0.05	763	763				
A	724.6	−2.4	−0.11	779	0.8	0.03						
B	748.4	−2.3	−0.10	800	1.0	0.04	798	800				
B	749.4	−0.6	−0.03	817	1.1	0.04						
B	756.0	1.1	0.05	828	−1.5	−0.05						

[a]Data were obtained by fitting the wavenumbers up to 3 GPa. The corresponding Grüneisen parameters (γ) were calculated by the function $\gamma = (B_0/\omega_0)\cdot(d\omega/dP)$ using B_0 = 29.8 GPa obtained from the HP-XRD data. For the sake of simplicity, here we only provide the calculated vibrational modes, which have been tentatively attributed to the experimentally observed Raman- and IR-active modes. The total number of calculated vibrational modes (108) can be found in the Supporting Information (Table S1).

https://doi.org/10.1021/acs.jpcc.1c04659
J. Phys. Chem. C 2021, 125, 17448−17461

between the modes below 500 cm^{-1} and the part of the spectrum above 700 cm^{-1}. In this work, we have detected 21 Raman-active modes in $Co(IO_3)_2$ in contrast to previous studies reporting only 15 modes.[18,19] The agreement between different experiments is good. According to group theory, all 18 independent atoms in $Co(IO_3)_2$ are located in 2*a* Wyckoff sites, resulting in 108 vibrational modes (54A + 54B). Since both are polar modes, all of them are both Raman- and IR-active; therefore, up to 216 modes could be observed in the IR spectra due to the TO−LO (transverse optical−longitudinal optical) splitting.

Experimentally, the strongest mode is found at 765 cm^{-1} in $Co(IO_3)_2$, a wavenumber almost identical to 763 cm^{-1} reported in the literature[18,19] and very close to that of the strongest mode in $Zn(IO_3)_2$ (782 cm^{-1}) and in $Fe(IO_3)_3$ (790 cm^{-1}).[14,16] The similar wavenumber of the strongest mode in metal iodates is reasonable since this mode can be related to an internal I−O stretching vibration of the IO_3 molecule, according to the vibrational modes of the pyramidal IO_3^- free ion.[47−50]

The comparison of the Raman spectra of iron, zinc, and cobalt iodates at ambient pressure with our DFT calculations[14,19] enables us to analyze the vibrations which produce the spectrum. The high-wavenumber part of $Co(IO_3)_2$ (wavenumber above 700 cm^{-1}) is likely associated with symmetric and asymmetric stretching I−O vibrations of the IO_3 molecule. According to a previous vibrational study of $Co(IO_3)_2$,[19] the most intense band near 762 cm^{-1} and the bands near 781 and 800 cm^{-1} are assigned to symmetric I−O stretching modes of the IO_6 molecule, whereas the 727 cm^{-1} mode was assigned to the asymmetric I−O stretching mode of the IO_6 molecule. This assignment is different from previous authors who attributed these modes to stretching modes of the pyramidal IO_3^- molecule.[47−50] Shen et al. attributed the modes of iodates between 779 and 826 cm^{-1} to the symmetric (ν_1) and asymmetric (ν_3) I−O stretching modes of the IO_3 molecule.[47] A similar assignment was performed by Dasent and Waddington.[48] In contrast, the modes at 775 and 805 cm^{-1} were assigned to the asymmetric (ν_3) and symmetric (ν_1) I−O stretching modes of the IO_3^- molecule by Gardiner et al.[49,50] Consequently, which of the symmetric or asymmetric stretching modes has the highest wavenumber seems to be controversial. In two recent studies, we have clarified that the strongest mode of metal iodates corresponds to the symmetric I−O stretching mode and that the asymmetric I−O stretching modes have a lower wavenumber than the symmetric I−O stretching modes.[14,16] Additionally, it must be clarified that the vibrational modes of the monoclinic $P2_1$ structure are not gerade and ungerade, as suggested in ref 19, and in fact they have the same number of A and B modes. Based on our DFT calculations (see Supporting Information, Figure S12), we have observed a mode at 727 cm^{-1} that can be assigned to an asymmetric stretching I−O vibration and the modes at 765, 779 (strongest mode), and 800 cm^{-1} can be assigned to a symmetric stretching I−O vibration in the IO_3 molecule, which is exactly the same as the assignment given in ref 19.

The bending modes of iodates are observed in the region from 300 to 500 cm^{-1}. In ref 19, the modes at 327, 353, and 392 cm^{-1} were assigned to a threefold degenerate symmetric bending mode and the 429 cm^{-1} mode to the asymmetric bending mode of the IO_6 molecule. Again, these assignments contrast with previous studies that attributed them to the pyramidal IO_3^- molecules. Modes at 330 and 390 cm^{-1} were attributed by Shen et al. to the asymmetric (ν_4) and symmetric (ν_2) bending modes of the IO_3^- molecule, respectively.[47] Similarly, modes above 400 cm^{-1} were also attributed to symmetric (ν_2) bending modes of the IO_3^- molecule.[48] Modes at 320 and 358 cm^{-1} were assigned to the asymmetric (ν_4) and symmetric (ν_2) bending modes of the IO_3^- molecule, respectively.[49] Therefore, it is clear that symmetric bending modes have higher wavenumbers than asymmetric bending modes in iodates as they occur in chlorates and bromates.[50] In our experiments, the bending modes of $Co(IO_3)_2$ are observed at 327, 354, 395, and 421 cm^{-1}, respectively. Based on the vibration symmetry of the corresponding calculated modes (see Supporting Information, Figure S13), the three modes with the lowest wavenumbers can be assigned to symmetric (ν_2) bending modes of the IO_3^- molecule, and the modes around 421 cm^{-1} can be assigned to the asymmetric (ν_4) bending modes of the IO_3^- molecule, again in agreement with the assignment in ref 19. Finally, the modes below 300 cm^{-1} have been associated with the translational and rotational motions of the iodate as a rigid unit.

Results of HP-RS experiments on $Co(IO_3)_2$ at selected pressures up to 23.4 GPa are shown in Figure 8. The spectra

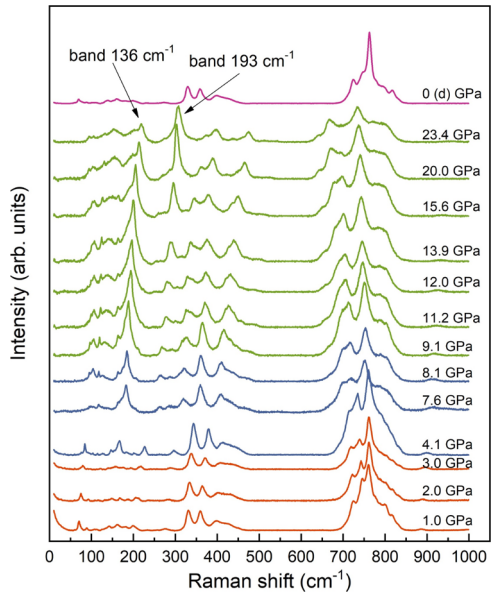

Figure 8. HP-RS spectra of $Co(IO_3)_2$ at selected pressures. The "d" in the top pattern means that it is collected during the decompression process. Here, the Raman spectra of different phases are shown in different colors (ambient-pressure phase-orange, I1 phase-blue, and I2 phase-green). The bands at 136 and 193 cm^{-1} determined at room pressure are also marked in the figure.

can be separated into two parts: wavenumber above 700 cm^{-1} and wavenumber below 500 cm^{-1}, with a phonon gap of more than 200 cm^{-1} at ambient pressure. Up to the highest pressure, there is no evidence of the occurrence of a first-order phase transition. Moreover, the Raman spectrum collected at ambient pressure after decompression (top spectrum in Figure 8) is like that obtained before the compression process (Figure 7), thus suggesting that pressure-induced structural changes up to 23 GPa are fully reversible. Apparently, there is a significant intensity increase of phonons at 136 and 193 cm^{-1} at ambient pressure, which shift to 220 and 307 cm^{-1} at 23.4 GPa. The intensity of the peak at 136 cm^{-1} (labeled in Figure 8)

https://doi.org/10.1021/acs.jpcc.1c04659
J. Phys. Chem. C 2021, 125, 17448−17461

increases to its highest level at 13.9 GPa and then decreases with further compression, whereas the intensity of the peak at 193 cm^{-1} increases continuously to the highest pressure and even surpasses the most intense band 762 cm^{-1} at the highest pressure. We plot the relative intensity ratio between the modes at 136 and 193 cm^{-1} in Figure 9. An evident change can

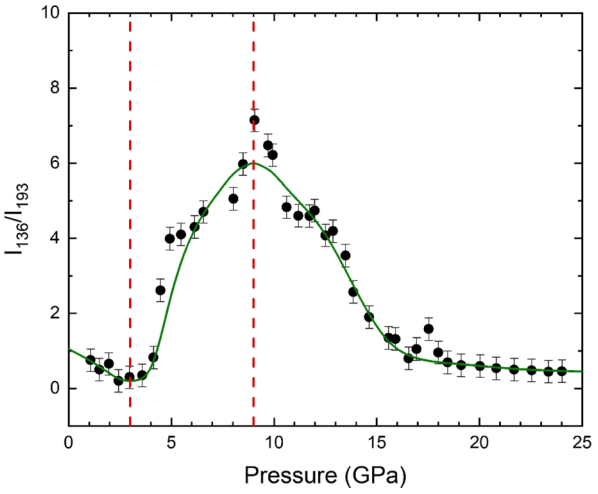

Figure 9. Relative Raman intensity ratio of the modes at 136 and 193 cm^{-1} as a function of pressure. The solid circles are the experimental data, while the green line is a guide for the eye. The orange dashed line marks the pressure of the phase transition.

be found at around 3 GPa, from a negative or even zero slope to a positive one, and at 9 GPa from a positive to negative slope, respectively. In general, the Raman spectrum can suffer a change of the peak intensity under pressure due to a change in the Raman scattering cross section of the different modes. Pressure can also affect the intensity of first-order Raman phonons, which mainly depend on the Hamiltonian matrix elements of electron−photon and electron−phonon interactions responsible for the Raman effect.[51,52] In this context, pressure-induced changes of Raman intensities usually are related to changes in the high-order susceptibility tensor of the material, which can be typical of certain Raman modes. In particular, structural changes leading to first-, second-, or higher-order pressure-induced phase transitions can alter the Raman intensity. Moreover, the presence of precursor effects of pressure-induced phase transitions or pressure-induced amorphization can also modify the Raman intensities. Additionally, the loss of perfect hydrostatic conditions with the emergence of pressure gradients, the change of the absorption coefficient under compression, and the presence of resonant Raman scattering can also affect the intensity of Raman peaks. In our case, we think the intensity change of bands at 136 and 193 cm^{-1} is induced by the two isostructural phase transitions identified by HP-XRD measurements. These two transitions also lead to changes in the pressure dependence of the Raman wavenumbers as we will discuss in the next paragraph.

The theoretical and experimental Raman-active modes of $Co(IO_3)_2$ as a function of pressure are shown in Figure 10 (and in Supporting Information, Figures S15−S17). The most notable features are as follows: (i) the pressure-induced reduction of the phonon gap (ca. between 450 and 700 cm^{-1} at room pressure) both in experiments and DFT calculations. The closing of the phonon gap is a result of the blue shift of the modes below 450 cm^{-1} and the red shift (softening) of the modes above 700 cm^{-1}. Usually, phonon softening is a sign of dynamic instability and may induce a crystalline−crystalline phase transition or an amorphization.[53] (ii) Some modes of the high-wavenumber region, which correspond to I−O stretching modes of IO_3^- units, show a soft behavior in the low-pressure and I1 phase, as occurs with other metal iodates.[14,16,39] In order to accommodate the three additional oxyanions, the bond distance between iodine and the three original oxyanions will slightly increase under compression, and under a harmonic approximation, there is a linear relationship between the $\omega^{-2/3}$, where ω represented the soft modes, and the calculated average I−O bond length, which has been proven in $Fe(IO_3)_3$ and $Zn(IO_3)_2$.[14,16] Therefore, the softening of several high-wavenumber modes in $Co(IO_3)_2$ under pressure is due to the

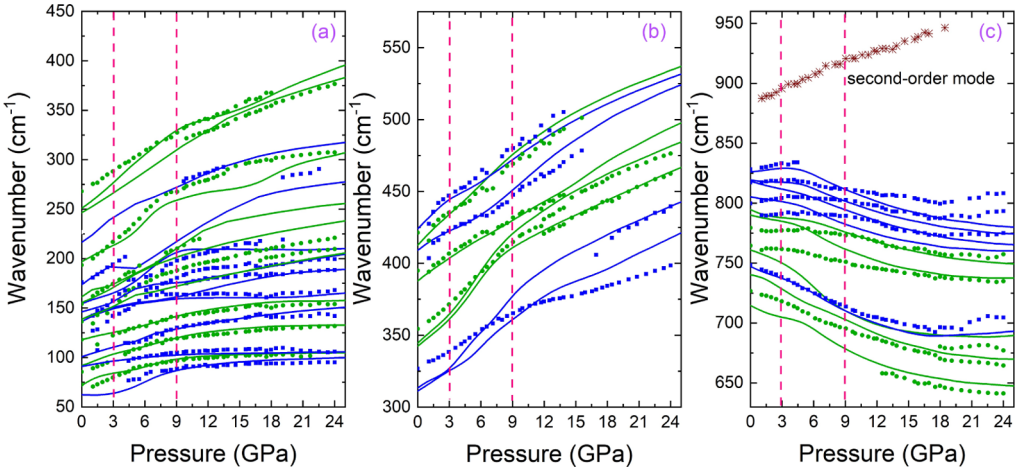

Figure 10. Pressure dependence of the Raman-active wavenumbers in $Co(IO_3)_2$. Different panels show different wavelength regions. Experiments are shown with symbols and calculations with lines. A- and B-symmetry modes are shown in green and blue, respectively. For the sake of clarity, here we show the theoretical modes tentatively attributed to the experimentally observed modes. In the Supporting Information, we include figures with all calculated modes. Vertical pink dashed lines indicate the suggested transition pressures corresponding to the two isostructural phase transitions we found in HP-XRD. In the highest wavenumber region, we apply the offset of 70 cm^{-1} to calculate wavenumbers to match experimental wavenumbers as described in the text.

https://doi.org/10.1021/acs.jpcc.1c04659
J. Phys. Chem. C 2021, 125, 17448−17461

slight enlargement of the shorter I−O bond distances under compression. (iii) Slope coefficient changes are found in almost every vibrational mode near 3 and 9 GPa. From the experimental side, this can be clearly recognized in the modes at 118, 193, and 327 cm^{-1} that exhibit a non-linear behavior. Qualitatively similar pressure dependence of the Raman modes has also been found in $Fe(IO_3)_3$[14] and $Zn(IO_3)_2$,[16] and other materials containing LEPs, such as β-Bi_2O_3,[54,55] Sb_2S_3,[56] α-As_2Te_3,[57] $SbPO_4$,[58] and As_2S_3,[59] and alkali-metal bismuth iodate $Na_3Bi(IO_3)_6$.[39] The observed non-linear behavior of the Raman modes gives further evidence of the two isostructural phase transitions we found in HP-XRD data. (iv) There are several low-wavenumber modes in both experimental and calculated modes with very high Grüneisen parameters, even exceeding the value of 2 (see Table 3). These high values indicate that many vibrational modes have a very high anharmonic contribution that is uncommon in covalent and ionic compounds.

Infrared Study. High-pressure Fourier transform infrared (HP-FTIR) spectra between 200 and 600 cm^{-1} on $Co(IO_3)_2$ are shown in Figure 11 at selected pressures up to 18.6 GPa.

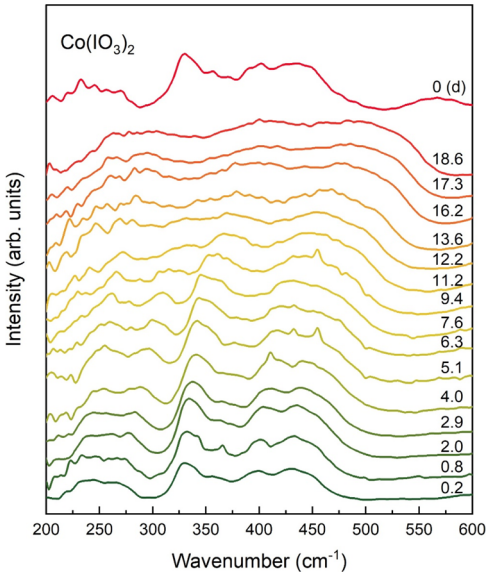

Figure 11. HP-FTIR spectra of $Co(IO_3)_2$ at selected pressures. The "d" in the top spectrum means that it is collected during the decompression process. The pressure of each pattern is shown on the right in "GPa".

Nine modes have been detected at the lowest pressure (0.2 GPa). They are summarized in Table 3 and compared with previously reported IR data, together with a tentative mode assignment based on the theoretical calculated modes symmetries. The pressure coefficients are also shown in Table 3. They were obtained via a linear fit to data in the 0−3 GPa range. The detected IR-active modes are consistent with the values reported in ref 19; however, two modes near 208 and 250 cm^{-1} reported in ref 19 are missing in our experiment. The possible reason could be the merging with neighboring strong peaks at HP. Notably, the peaks become significantly broader at HP (above around 12 GPa), likely due to the loss of the hydrostatic conditions in the solid PTM (Cesium iodide, CsI).[60] For this reason, we have only followed the center of the absorption bands that contain more than one phonon. From the FTIR data collected at 0 GPa after downstroke (see the top spectrum of Figure 11), we can confirm that the structural changes of $Co(IO_3)_2$ up to the highest pressure in our experiment (22.3 GPa) are fully reversible, in agreement with HP-XRD and HP-RS measurements.

Some theoretically predicted vibrational modes that have not been detected in the Raman spectra can be found in the IR spectra (see Table 3), a fact that confirms the complementarity of these two techniques. IR-active modes at 327, 355, and 399 cm^{-1} were previously attributed to the triply degenerate symmetric bending mode of IO_6, whereas the mode at 421 cm^{-1} was attributed to the asymmetric bending of IO_6.[19] We have measured modes at 331, 357, and 397 cm^{-1} that have been assigned to the symmetric (ν_2) bending modes of the IO_3^- molecule, whereas the mode at 427 cm^{-1} has been attributed to the asymmetric (ν_4) bending mode of the IO_3^- molecule, thus in a good agreement with the previous study. Additionally, modes below 300 cm^{-1} can be associated with the translation and rotational motions.

The pressure dependence of the theoretical and experimental IR-active mode wavenumbers in $Co(IO_3)_2$ are plotted together in Figure 12. All modes harden under pressure and a

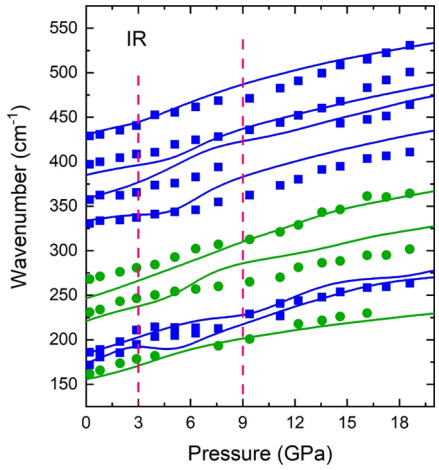

Figure 12. Pressure dependence of the IR-active wavenumbers in $Co(IO_3)_2$. Symbols correspond to experimental data while lines correspond to theoretically calculated data. A- and B-symmetries are represented by green and blue colors, respectively. Vertical pink dashed lines indicate suggested transition pressures. For the whole calculated IR-active modes in that region, the reader can find it in the Supporting Information, Figure S14.

change in the pressure coefficients of all modes can be observed at 3.0 and 9.0 GPa. The change is clearer in the three experimental modes with the lowest wavenumbers. The non-linear pressure dependence exhibited by the wavenumbers of the IR modes is like that of the Raman-active modes, thus providing further evidence of the two subtle symmetry-preserving phase transitions we have previously described. It can be also mentioned that the non-linear pressure dependence of the IR-active modes has also been reported for $Zn(IO_3)_2$ as evidence of the presence of isostructural phase transitions.[61]

To conclude, we must emphasize two aspects of this work. The first point is that isostructural phase transitions seem to be a common feature of a number of compounds featuring strong stereoactive cation or anion LEPs since they have been recently characterized in group-15 oxides and chalcogenides such as β-Bi_2O_3,[54,55] As_2S_3,[59] and $SbPO_4$[58] and in several

https://doi.org/10.1021/acs.jpcc.1c04659
J. Phys. Chem. C 2021, 125, 17448−17461

iodates, as discussed here. In fact, many of these isostructural phase transitions seem to be of second-order or even of higher-order according to Ehrenfest's classification, and they can even appear as hidden or internal isostructural phase transitions, as recently reported for β-Sb_2O_3.[62]

The second point is that the short I−O bond distances increase in length under compression, the long I−O bond distances decrease in length in order to form a highly symmetric structure with very similar I−O bond distances and higher coordination at high pressure, and the presence of very high Grüneisen parameters and the softening of many high-wavenumber modes leading to phonon gap closing [as observed in the three metal iodates, $Co(IO_3)_2$, $Zn(IO_3)_2$, and $Fe(IO_3)_3$] are features similar to those recently reported in an HP study of As_2S_3, a compound featuring a strong stereoactive cation LEP with threefold coordination for As at room pressure.[59] These features have been related to the novel phenomenon of "metavalent" bonding; that is, the observation of a new type of an intermediate chemical bonding between covalent and metallic bonding, which is characterized by bonds with less than two electrons per bond.[63−65] It has been proved that metavalent bonding at room pressure is found in binary and ternary compounds of IV−VI and V_2−VI_3 families with 5 and 6 cation coordination (GeTe, SnTe, PbS, PbSe, PbTe, β-As_2Te_3, Sb_2Te_3, Bi_2Se_3, Bi_2Te_3, and rhombohedral $GeSb_2Te_4$, rhombohedral $SnSb_2Te_4$[65,66] and by extension in rhombohedral $GeBi_2Te_4$ and rhombohedral $SnBi_2Te_4$). Additionally, it has been proven that this kind of bonding develops at HP in compounds of IV−VI and V_2−VI_3 families with a smaller coordination at room pressure (GeSe,[67] As_2S_3,[59] and related compounds). Recently, it has been suggested that metavalent bonding also occurs in halide perovskites,[68] thus opening the door to explore metavalent bonding in halide-related compounds such as metal iodates. However, in order to fully prove the presence of metavalent bonding in iodates at HP, calculations of the electronic density of I−O bonds, Born effective charges of I atoms, and optical dielectric constants under pressure will be required. Such calculations are beyond the scope of this work even if they are already planned for a more comprehensive study on this topic.

CONCLUSIONS

We have reported a joint experimental and theoretical study of the structural and vibrational properties of $Co(IO_3)_2$ under compression. We have observed compelling evidence of two reversible pressure-induced isosymmetric phase transitions at 3.0 GPa and in the pressure range of 9.0−11.0 GPa by means of HP-XRD, HP-RS, and HP-FTIR measurements and DFT calculations.

The unit cell of $Co(IO_3)_2$ shows a huge anisotropic compressibility, with the *b*-axis being the most compressible axis and largely determining the bulk moduli of 29.8 and 70.8 GPa in experiments (32.1 and 50.7 GPa in theoretical calculation) for the ambient + I1 and I2 phases, respectively. Moreover, the bulk modulus of the ambient pressure phase of $Co(IO_3)_2$ has been proven to be dominated by the large compressibility of the IO_6 polyhedra rather than that of the CoO_6 units.

A non-linear pressure dependence of Raman- and IR-active mode wavenumbers of $Co(IO_3)_2$ has been measured with soft high-wavenumber Raman modes, leading to a closing of the phonon gap under compression. The vibrational properties of $Co(IO_3)_2$ under compression are qualitatively similar to those of $Fe(IO_3)_3$ and $Zn(IO_3)_2$, suggesting that these features are common to metal iodates with IO_3^- units.

The unit-cell parameters and volume deduced from the refinements of the HP-XRD data, as well as the Raman- and IR-active mode wavenumbers, exhibit a non-linear pressure dependence, indicating the presence of two symmetry-preserving phase transitions at 3.0 GPa and in the pressure range of 9.0−11.0 GPa. The theoretically calculated pressure dependence of the I−O and Co−O bond distances in $Co(IO_3)_2$ and its comparison with the bond distances previously reported for $Fe(IO_3)_3$ and $Zn(IO_3)_2$ allow us to conclude that the mechanism driving the two isostructural phase transitions is the lattice instability caused by the gradual coordination increase of iodine that in turn is related to the decrease of the stereoactivity of the LEP at HP. The decrease of three long I−O bond distances forces an increase of the three short I−O bond distances to accommodate the additional bonds, leading to the observed phase transitions. Because of the increase of the short I−O bonds, there is a softening of all the I−O stretching modes of the IO_3^- molecule. Additional support for the two transitions comes from the dramatic change of phonons' relative intensity ratio between 136 and 193 cm^{-1} in Raman spectra. Therefore, this work shows once again that isostructural phase transitions are common to compounds featuring strong LEPs.

The softening of the stretching modes and the large pressure coefficients of the bending modes, the concurrent increase of the short I−O bonds, and decrease of the long I−O bond distances leading to a high symmetry of the I2 HP phase (like the huge decrease on the distortion index of IO_6 polyhedra) suggest that these changes are probably related to the formation of pressure-induced metavalent bonding in metal iodates.

ASSOCIATED CONTENT

Supporting Information

The Supporting Information is available free of charge at https://pubs.acs.org/doi/10.1021/acs.jpcc.1c04659.

Microscopic image of the sample, Rietveld refinement of the XRD data collected at ambient pressure and high pressure, pressure dependence of the *d*-spacing, comparison of the lattice parameter and volume between $Zn(IO_3)_2$ and $Co(IO_3)_2$, atomic movement of some Raman modes, all the experimental and calculated pressure dependences of the Raman and infrared modes, and all the experiment- and calculation-determined modes and related information at ambient pressure (PDF)

AUTHOR INFORMATION

Corresponding Author

A. Liang − *Departamento de Física Aplicada-ICMUV-MALTA Consolider Team, Universitat de València, 46100 Burjassot (Valencia), Spain;* orcid.org/0000-0002-0515-0484; Email: Akun2.Liang@uv.es

Authors

C. Popescu − *CELLS-ALBA Synchrotron Light Facility, 08290 Barcelona, Spain*

F. J. Manjon − *Instituto de Diseño para la Fabricación y Producción Automatizada, MALTA Consolider Team,*

Universitat Politècnica de València, 46022 València, Spain; orcid.org/0000-0002-3926-1705

R. Turnbull − *Departamento de Física Aplicada-ICMUV-MALTA Consolider Team, Universitat de València, 46100 Burjassot (Valencia), Spain*

E. Bandiello − *Departamento de Física Aplicada-ICMUV-MALTA Consolider Team, Universitat de València, 46100 Burjassot (Valencia), Spain;* orcid.org/0000-0003-0956-3195

P. Rodriguez-Hernandez − *Departamento de Física and Instituto de Materiales y Nanotecnología, MALTA Consolider Team, Universidad de La Laguna, 38206 La Laguna, Spain*

A. Muñoz − *Departamento de Física and Instituto de Materiales y Nanotecnología, MALTA Consolider Team, Universidad de La Laguna, 38206 La Laguna, Spain;* orcid.org/0000-0003-3347-6518

I. Yousef − *CELLS-ALBA Synchrotron Light Facility, 08290 Barcelona, Spain;* orcid.org/0000-0001-7818-8611

Z. Hebboul − *Laboratoire Physico-Chimie des Matériaux (LPCM), University Amar Telidji of Laghouat, Laghouat 03000, Algeria*

D. Errandonea − *Departamento de Física Aplicada-ICMUV-MALTA Consolider Team, Universitat de València, 46100 Burjassot (Valencia), Spain;* orcid.org/0000-0003-0189-4221

Complete contact information is available at: https://pubs.acs.org/10.1021/acs.jpcc.1c04659

Notes

The authors declare no competing financial interest.

■ ACKNOWLEDGMENTS

This work was supported by the Generalitat Valenciana under Project PROMETEO 2018/123-EFIMAT and by the Spanish Ministerio de Ciencia, Universidades, e Investigación under Projects PID2019-106383GB-41/42/43, as well as through MALTA Consolider Team research network (RED2018-102612-T). A.M. and P.R.-H. acknowledge computing time provided by Red Española de Supercomputación (RES) and the MALTA Consolider Team cluster. D.E. acknowledges the resources and technical assistance provided by the Informatics Service of Universitat de Valencia through the Tirant III cluster. A.L. and D.E. would like to thank the Generalitat Valenciana for the Ph.D. Fellowship no. GRISOLIAP/2019/025. R.T. acknowledges funding from the Spanish Ministerio de Economía y Competitividad (MINECO) via the Juan de la Cierva Formación fellowship (FJC2018-036185-I). C.P. is thankful for the financial support of the Spanish Mineco Project no. FIS2017-83295-P. E.B would like to thank the University of Valencia for his "Attracció de Talent" postdoctoral contract (UV-INV_POSTDOC19-1026935). The authors thank Sandrine Beauquis from Symme, Université Savoie Mont Blanc (France), for her technical assistance concerning the SEM and ADX analyses. PXRD experiments were performed at the MSPD beamline of ALBA Synchrotron (experiment no. 2019083663). IR experiments were performed at the MIRAS beamline of ALBA Synchrotron (experiment no. 2020024118).

■ REFERENCES

(1) Bergman, J. G.; Boyd, G. D.; Ashkin, A.; Kurtz, S. K. New Nonlinear Optical Materials: Metal Oxides with Nonbonded Electrons. *J. Appl. Phys.* **1969**, *40*, 2860−2863.

(2) Ok, K. M.; Chi, E. O.; Halasyamani, P. S. Bulk Characterization Methods for Non-Centrosymmetric Materials: Second-Harmonic Generation, Piezoelectricity, Pyroelectricity, and Ferroelectricity. *Chem. Soc. Rev.* **2006**, *35*, 710−717.

(3) Wang, C.; Zhang, T.; Lin, W. Rational Synthesis of Noncentrosymmetric Metal-Organic Frameworks for Second-Order Nonlinear Optics. *Chem. Rev.* **2012**, *112*, 1084−1104.

(4) Phanon, D.; Gautier-Luneau, I. Promising Material for Infrared Nonlinear Optics: NaI_3O_8 Salt Containing an Octaoxotriiodate(V) Anion Formed from Condensation of $[IO_3]^-$ Ions. *Angew. Chem., Int. Ed.* **2007**, *46*, 8488−8491.

(5) Phanon, D.; Mosset, A.; Gautier-Luneau, I. New Materials for Infrared Non-Linear Optics. Syntheses, Structural Characterisations, Second Harmonic Generation and Optical Transparency of M(IO3)3 Metallic Iodates. *J. Mater. Chem.* **2007**, *17*, 1123−1130.

(6) Kang, M. O.; Halasyamani, P. S. New Metal Iodates: Syntheses, Structures, and Characterizations of Noncentrosymmetric La(IO3)3 and NaYl4O 12 and Centrosymmetric *β*-Cs2I4O 11 and Rb2I6O15-(OH) 2·H2O. *Inorg. Chem.* **2005**, *44*, 9353−9359.

(7) Dmitriev, V. G.; Gurzadyan, G. G.; Nikogosyan, D. N. *Handbook of Nonlinear Optical Crystals*, 3rd ed.; Springer, 2013.

(8) Bentria, B.; Benbertal, D.; Bagieu-Beucher, M.; Mosset, A.; Zaccaro, J. Crystal Engineering Strategy for Quadratic Nonlinear Optics. Part II: Hg(IO3)2. *Solid State Sci.* **2003**, *5*, 359−365.

(9) Huang, Y.; Meng, X.; Gong, P.; Yang, L.; Lin, Z.; Chen, X.; Qin, J. $A_2BiI_5O_{15}$ (A = K+ or Rb +): Two New Promising Nonlinear Optical Materials Containing $[I_3O_9]_3^-$ Bridging Anionic Groups. *J. Mater. Chem. C* **2014**, *2*, 4057−4062.

(10) Xu, X.; Hu, C.-L.; Li, B.-X.; Yang, B.-P.; Mao, J.-G. A-AgI_3O_8 and B-AgI_3O_8 with Large SHG Responses: Polymerization of IO_3 Groups into the I_3O_8 Polyiodate Anion. *Chem. Mater.* **2014**, *26*, 3219−3230.

(11) Bu, K.; Luo, H.; Guo, S.; Li, M.; Wang, D.; Dong, H.; Ding, Y.; Yang, W.; Lü, X. Pressure-Regulated Dynamic Stereochemical Role of Lone-Pair Electrons in Layered Bi2O2S. *J. Phys. Chem. Lett.* **2020**, *11*, 9702−9707.

(12) Bayarjargal, L.; Wiehl, L.; Friedrich, A.; Winkler, B.; Juarez-Arellano, E. A.; Morgenroth, W.; Haussühl, E. Phase Transitions in KIO_3. *J. Phys.: Condens. Matter* **2012**, *24*, 325401.

(13) Suffren, Y.; Gautier-Luneau, I.; Darie, C.; Goujon, C.; Legendre, M.; Leynaud, O. First Evidence of a Phase Transition in a High-Pressure Metal Iodate: Structural and Thermal Studies of $AgIO_3$ Polymorphs. *Eur. J. Inorg. Chem.* **2013**, *2013*, 3526−3532.

(14) Liang, A.; Rahman, S.; Rodriguez-Hernandez, P.; Muñoz, A.; Manjón, F. J.; Nenert, G.; Errandonea, D. High-Pressure Raman Study of $Fe(IO_3)_3$: Soft-Mode Behavior Driven by Coordination Changes of Iodine Atoms. *J. Phys. Chem. C* **2020**, *124*, 21329−21337.

(15) Liang, A.; Rahman, S.; Saqib, H.; Rodriguez-Hernandez, P.; Muñoz, A.; Nénert, G.; Yousef, I.; Popescu, C.; Errandonea, D. First-Order Isostructural Phase Transition Induced by High-Pressure in $Fe(IO_3)_3$. *J. Phys. Chem. C* **2020**, *124*, 8669−8679.

(16) Liang, A.; Popescu, C.; Manjon, F. J.; Muñoz, A.; Hebboul, Z.; Errandonea, D. Structural and Vibrational Study of $Zn(IO_3)_2$ Combining High-Pressure Experiments and Density-Functional Theory. *Phys. Rev. B* **2021**, *103*, 054102.

(17) Phanon, D.; Bentria, B.; Jeanneau, E.; Benbertal, D.; Mosset, A.; Gautier-Luneau, I. Crystal Structure of $M(IO_3)_2$ Metal Iodates, Twinned by Pseudo-Merohedry, with MII: MgII, MnII, CoII, NiII and ZnII. *Z. Kristallogr.* **2006**, *221*, 635−642.

(18) Pracht, G.; Lutz, H. D. Phase Relationships in Cobalt Iodate Hydrates - Thermal Analyses, X-Ray, IR, and Raman Spectroscopic Studies. *Thermochim. Acta* **2000**, *354*, 153−160.

(19) Kochuthresia, T. C.; Gautier-Luneau, I.; Vaidyan, V. K.; Bushiri, M. J. Raman and Ftir Spectral Investigations of Twinned

M(IO3)2 (M = Mn, Ni, Co, AND Zn) Crystals. *J. Appl. Spectrosc.* **2016**, *82*, 941−946.
(20) Rietveld, H. M. A Profile Refinement Method for Nuclear and Magnetic Structures. *J. Appl. Crystallogr.* **1969**, *2*, 65−71.
(21) Fauth, F.; Peral, I.; Popescu, C.; Knapp, M. The New Material Science Powder Diffraction Beamline at ALBA Synchrotron. *Powder Diffr.* **2013**, *28*, S360−S370.
(22) Prescher, C.; Prakapenka, V. B. DIOPTAS: A Program for Reduction of Two-Dimensional X-Ray Diffraction Data and Data Exploration. *High Pressure Res.* **2015**, *35*, 223−230.
(23) Dewaele, A.; Loubeyre, P.; Mezouar, M. Equations of State of Six Metals above 94 GPa. *Phys. Rev. B: Condens. Matter Mater. Phys.* **2004**, *70*, 094112.
(24) Palik, E. D. *Handbook of Optical Constants of Solid*; Academic Press: Maryland, 1997.
(25) Mao, H. K.; Xu, J.; Bell, P. M. Calibration of the Ruby Pressure Gauge to 800 Kbar under Quasi-Hydrostatic Conditions. *J. Geophys. Res.: Solid Earth* **1986**, *91*, 4673−4676.
(26) Yousef, I.; Ribó, L.; Crisol, A.; Šics, I.; Ellis, G.; Ducic, T.; Kreuzer, M.; Benseny-Cases, N.; Quispe, M.; Dumas, P.; et al. MIRAS: The Infrared Synchrotron Radiation Beamline at ALBA. *Synchrotron Radiat. News* **2017**, *30*, 4−6.
(27) Hohenberg, P.; Kohn, W. Inhomogeneous Electron Gas. *Phys. Rev.* **1964**, *136*, B864−B871.
(28) Kresse, G.; Furthmüller, J. Efficiency of Ab-Initio Total Energy Calculations for Metals and Semiconductors Using a Plane-Wave Basis Set. *Comput. Mater. Sci.* **1996**, *6*, 15−50.
(29) Kresse, G.; Hafner, J. Ab Initio Molecular Dynamics for Liquid Metals. *Phys. Rev. B: Condens. Matter Mater. Phys.* **1993**, *47*, 558−561.
(30) Blöchl, P. E. Projector Augmented-Wave Method. *Phys. Rev. B: Condens. Matter Mater. Phys.* **1994**, *50*, 17953−17979.
(31) Perdew, J. P.; Ruzsinszky, A.; Csonka, G. I.; Vydrov, O. A.; Scuseria, G. E.; Constantin, L. A.; Zhou, X.; Burke, K. Restoring the Density-Gradient Expansion for Exchange in Solids and Surfaces. *Phys. Rev. Lett.* **2008**, *100*, 136406.
(32) Mattsson, A. E.; Armiento, R. Implementing and Testing the AM05 Spin Density Functional. *Phys. Rev. B: Condens. Matter Mater. Phys.* **2009**, *79*, 155101.
(33) Dudarev, S. L.; Botton, G. A.; Savrasov, S. Y.; Humphreys, C. J.; Sutton, A. P. Electron-Energy-Loss Spectra and the Structural Stability of Nickel Oxide:An LSDA+U Study. *Phys. Rev. B: Condens. Matter Mater. Phys.* **1998**, *57*, 1505−1509.
(34) Jain, A.; Ong, S. P.; Hautier, G.; Chen, W.; Richards, W. D.; Dacek, S.; Cholia, S.; Gunter, D.; Skinner, D.; Ceder, G.; et al. Commentary: The Materials Project: A Materials Genome Approach to Accelerating Materials Innovation. *APL Mater.* **2013**, *1*, 011002.
(35) Togo, A.; Tanaka, I. First Principles Phonon Calculations in Materials Science. *Scr. Mater.* **2015**, *108*, 1−5.
(36) Klotz, S.; Chervin, J.-C.; Munsch, P.; Le Marchand, G. Hydrostatic Limits of 11 Pressure Transmitting Media. *J. Phys. D: Appl. Phys.* **2009**, *42*, 075413.
(37) Errandonea, D.; Meng, Y.; Somayazulu, M.; Häusermann, D. Pressure-Induced → ω Transition in Titanium Metal: A Systematic Study of the Effects of Uniaxial Stress. *Phys. B* **2005**, *355*, 116−125.
(38) Le Bail, A. Whole Powder Pattern Decomposition Methods and Applications: A Retrospection. *Powder Diffr.* **2005**, *20*, 316−326.
(39) Song, H.; Jiang, D.; Wang, N.; Xing, W.; Guo, R.; Lin, Z.; Yao, J.; Wang, Y.; Tu, H.; Zhang, G. Na3Bi(IO3)6: An Alkali-Metal Bismuth Iodate with Intriguing One-Dimensional [BiI6O18] Chains and Pressure-Induced Structural Transition. *Inorg. Chem.* **2021**, *60*, 2893−2898.
(40) Momma, K.; Izumi, F. VESTA 3 for Three-Dimensional Visualization of Crystal, Volumetric and Morphology Data. *J. Appl. Crystallogr.* **2011**, *44*, 1272−1276.
(41) Krapp, A.; Bickelhaupt, F. M.; Frenking, G. Orbital Overlap and Chemical Bonding. *Chem. - Eur. J.* **2006**, *12*, 9196−9216.
(42) Murnaghan, F. D. The Compressibility of Media under Extreme Pressures. *Proc. Natl. Acad. Sci. U.S.A.* **1944**, *30*, 244−247.
(43) Birch, F. Finite Elastic Strain of Cubic Crystals. *Phys. Rev.* **1947**, *71*, 809−824.
(44) Angel, R. J.; Alvaro, M.; Gonzalez-Platas, J. EosFit7c and a Fortran Module (Library) for Equation of State Calculations. *Z. Kristallogr. - Cryst. Mater.* **2014**, *229*, 405−419.
(45) Zhang, W. W.; Cui, Q. L.; Pan, Y. W.; Dong, S. S.; Liu, J.; Zou, G. T. High-Pressure x-Ray Diffraction Study of $LiIO_3$ to 75 GPa. *J. Phys.: Condens. Matter* **2002**, *14*, 10579−10582.
(46) Hebboul, Z.; Galez, C.; Benbertal, D.; Beauquis, S.; Mugnier, Y.; Benmakhlouf, A.; Bouchenafa, M.; Errandonea, D. Synthesis, Characterization, and Crystal Structure Determination of a New Lithium Zinc Iodate Polymorph LiZn(IO3)3. *Crystals* **2019**, *9*, 464.
(47) Shen, S. T.; Yao, Y. T.; Wu, T.-Y. Depolarization of Raman Lines and Structure of Chlorate, Bromate and Iodate Ions. *Phys. Rev.* **1937**, *51*, 235.
(48) Dasent, W. E.; Waddington, T. C. 491. Iodine-Oxygen Compounds. Part I. Infrared Spectra and Structure of Iodates. *J. Chem. Soc.* **1960**, *491*, 2429−2432.
(49) Gardiner, D. J.; Girling, R. B.; Hester, R. E. Vibrational Spectra and Force Constants of Chlorate, Bromate and Iodate Ions in Aqueous Solution. *J. Mol. Struct.* **1972**, *13*, 105−114.
(50) Nakamoto, K. Infrared and Raman Spectra of Inorganic and Coordination Compounds. *Handbook of Vibrational Spectroscopy*; American Cancer Society, 2006; p 115.
(51) Debernardi, A.; Ulrich, C.; Syassen, K.; Cardona, M. Raman Linewidths of Optical Phonons in 3c-Sic under Pressure: First-Principles Calculations and Experimental Results. *Phys. Rev. B: Condens. Matter Mater. Phys.* **1999**, *59*, 6774−6783.
(52) Lucazeau, G. Effect of Pressure and Temperature on Raman Spectra of Solids: Anharmonicity. *J. Raman Spectrosc.* **2003**, *34*, 478−496.
(53) Manjón, F. J.; Rodríguez-Hernández, P.; Muñoz, A.; Romero, A. H.; Errandonea, D.; Syassen, K. Lattice Dynamics of YVO_4 at High Pressures. *Phys. Rev. B: Condens. Matter Mater. Phys.* **2010**, *81*, 075202.
(54) Pereira, A. L. J.; Sans, J. A.; Vilaplana, R.; Gomis, O.; Manjón, F. J.; Rodríguez-Hernández, P.; Muñoz, A.; Popescu, C.; Beltrán, A. Isostructural Second-Order Phase Transition of β-Bi_2O_3 at High Pressures: An Experimental and Theoretical Study. *J. Phys. Chem. C* **2014**, *118*, 23189−23201.
(55) Pereira, A. L. J.; Errandonea, D.; Beltrán, A.; Gracia, L.; Gomis, O.; Sans, J. A.; García-Domene, B.; Miquel-Veyrat, A.; Manjón, F. J.; Muñoz, A.; et al. Structural Study of α-Bi_2O_3 under Pressure. *J. Phys.: Condens. Matter* **2013**, *25*, 475402.
(56) Ibáñez, J.; Sans, J. A.; Popescu, C.; López-Vidrier, J.; Elvira-Betanzos, J. J.; Cuenca-Gotor, V. P.; Gomis, O.; Manjón, F. J.; Rodríguez-Hernández, P.; Muñoz, A. Structural, Vibrational, and Electronic Study of Sb2S3 at High Pressure. *J. Phys. Chem. C* **2016**, *120*, 10547−10558.
(57) Cuenca-Gotor, V. P.; Sans, J. A.; Ibáñez, J.; Popescu, C.; Gomis, O.; Vilaplana, R.; Manjón, F. J.; Leonardo, A.; Sagasta, E.; Suárez-Alcubilla, A.; et al. Structural, Vibrational, and Electronic Study of α-As_2Te_3 under Compression. *J. Phys. Chem. C* **2016**, *120*, 19340−19352.
(58) Pereira, A. L. D. J.; Santamaría-Pérez, D.; Vilaplana, R.; Errandonea, D.; Popescu, C.; Da Silva, E. L.; Sans, J. A.; Rodríguez-Carvajal, J.; Muñoz, A.; Rodríguez-Hernández, P.; et al. Experimental and Theoretical Study of SbPO4 under Compression. *Inorg. Chem.* **2020**, *59*, 287−307.
(59) Cuenca-Gotor, V. P.; Sans, J. Á.; Gomis, O.; Mujica, A.; Radescu, S.; Muñoz, A.; Rodríguez-Hernández, P.; Da Silva, E. L.; Popescu, C.; Ibañez, J.; et al. Orpiment under Compression: Metavalent Bonding at High Pressure. *Phys. Chem. Chem. Phys.* **2020**, *22*, 3352−3369.
(60) Celeste, A.; Borondics, F.; Capitani, F. Hydrostaticity of Pressure-Transmitting Media for High Pressure Infrared Spectroscopy. *High Pressure Res.* **2019**, *39*, 608−618.
(61) Liang, A.; Turnbull, R.; Bandiello, E.; Yousef, I.; Popescu, C.; Hebboul, Z.; Errandonea, D. High-Pressure Spectroscopy Study of

$Zn(IO_3)_2$ Using Far-Infrared Synchrotron Radiation. *Crystals* **2021**, *11*, 34.
(62) Sans, J. A.; Manjón, F. J.; Pereira, A. L. d. J.; Ruiz-Fuertes, J.; Popescu, C.; Muñoz, A.; Rodríguez-Hernández, P.; Pellicer-Porres, J.; Cuenca-Gotor, V. P.; Contreras-García, J.; et al. Unveiling the Role of the Lone Electron Pair in Sesquioxides at High Pressure: Compressibility of β-Sb_2O_3. *Dalton Trans.* **2021**, *50*, 5493−5505.
(63) Wuttig, M.; Deringer, V. L.; Gonze, X.; Bichara, C.; Raty, J.-Y. Incipient Metals: Functional Materials with a Unique Bonding Mechanism. *Adv. Mater.* **2018**, *30*, 1803777.
(64) Raty, J. Y.; Schumacher, M.; Golub, P.; Deringer, V. L.; Gatti, C.; Wuttig, M. A Quantum-Mechanical Map for Bonding and Properties in Solids. *Adv. Mater.* **2019**, *31*, 1806280.
(65) Cheng, Y.; Wahl, S.; Wuttig, M. Metavalent Bonding in Solids: Characteristic Representatives, Their Properties, and Design Options. *Phys. Status Solidi RRL* **2021**, *15*, 2000482.
(66) Sans, J. A.; Vilaplana, R.; Da Silva, E. L.; Popescu, C.; Cuenca-Gotor, V. P.; Andrada-Chacón, A.; Sánchez-Benitez, J.; Gomis, O.; Pereira, A. L. J.; Rodríguez-Hernández, P.; et al. Characterization and Decomposition of the Natural van Der Waals SnSb2Te4 under Compression. *Inorg. Chem.* **2020**, *59*, 9900−9918.
(67) Xu, M.; Jakobs, S.; Mazzarello, R.; Cho, J.-Y.; Yang, Z.; Hollermann, H.; Shang, D.; Miao, X.; Yu, Z.; Wang, L.; et al. Impact of Pressure on the Resonant Bonding in Chalcogenides. *J. Phys. Chem. C* **2017**, *121*, 25447−25454.
(68) Wuttig, M.; Schön, C. F.; Schumacher, M.; Robertson, J.; Golub, P.; Bousquet, E.; Raty, J. Y. Halide Perovskites: Third Generation Photovoltaic Materials Empowered by Metavalent Bonding. **2020**, arXiv:2012.03794 (cond-mat), p 03794.

https://doi.org/10.1021/acs.jpcc.1c04659
J. Phys. Chem. C 2021, 125, 17448−17461